Magnetic imaging with spin-polarized low-energy electron microscopy

Nicolas Rougemaille, Andreas Schmid

EPJ AP

Applied Physics

EPJ.org
your physics journal

Eur. Phys. J. Appl. Phys. **50**, 20101 (2010) DOI: 10.1051/epjap/2010048

Magnetic imaging with spin-polarized low-energy electron microscopy

N. Rougemaille and A.K. Schmid

Eur. Phys. J. Appl. Phys. **50**, 20101 (2010)
DOI: 10.1051/epjap/2010048

THE EUROPEAN PHYSICAL JOURNAL APPLIED PHYSICS

Review Article

Magnetic imaging with spin-polarized low-energy electron microscopy

N. Rougemaille[1,a] and A.K. Schmid[2]

[1] Institut Néel, CNRS & Université Joseph Fourier, BP 166, 38042 Grenoble Cedex 9, France
[2] Lawrence Berkeley National Laboratory, 1 Cyclotron Road, Berkeley, CA 94720, USA

Received: 20 July 2009 / Accepted: 9 March 2010
Published online: 16 April 2010 –

Abstract. Spin-polarized low-energy electron microscopy (SPLEEM) is a technique for imaging magnetic microstructures at surfaces and in thin films. In this article, principles, advantages and limitations of SPLEEM are reviewed. Several recent studies illustrate how SPLEEM can be used to investigate spin reorientation transition phenomena, to determine magnetic domain configurations in low-dimensional structures, or to explore physics of magnetic couplings in layered systems. The work highlights the capability of the technique to reveal in situ and in real time quantitative information on micromagnetic configurations and structure-property relationships. In addition, spectroscopic reflectivity measurements with spin-polarized low-energy electron beams can be a useful tool to probe spin-dependent unoccupied band structure of magnetic materials and electronic properties of buried magnetic interfaces.

1 Introduction

To explore magnetic properties and phenomena in low-dimensional systems, tools that allow us to image magnetic domains and domain walls with spatial resolution down to the nanometer scale are important [1]. In the past decades, many microscopy techniques have been developed to image magnetism of bulk materials, thin layers, surfaces and interfaces [2]. These techniques include a range of different approaches:

- optical microscopies, where magneto-optic Kerr microscopy is one of the most widely known techniques [3,4];
- electron microscopies, including scanning electron microscopy with polarization analysis (SEMPA) [5,6], Lorentz microscopy [7,8], and electron holography [9,10];
- scanning probe microscopies such as magnetic force microscopy (MFM) [11,12], spin-polarized scanning tunneling microscopy (SP-STM) [13], or ballistic emission magnetic microscopy (BEMM) [14,15];
- soft X-rays microscopies, including X-ray photoemission electron microscopy (X-PEEM) [16,17] and scanning transmission X-ray microscopy (STXM) [18,19].

This far-from exhaustive list shows the remarkable progress made by the scientific community to develop, implement, and improve many complementary methods for imaging magnetic materials. For example, unprecedented spatial and temporal resolutions have been obtained recently: SP-STM now allows insights into magnetism down to the atomic scale [20,21], while magneto-optic Kerr microscopy has the potential to probe dynamic processes in the femtosecond range [22]. Moreover, the spectroscopic resolution of several microscopy techniques based on synchrotron radiation enables element-specificity and layer selective imaging of magnetic heterostructures [23,24].

The significant progress in magnetic imaging opens new windows into a host of scientific questions, including phenomena of nucleation and propagation of magnetic domains and domain walls, magnetic phase transitions, magnetic coupling in multilayers, magnetization dynamics, etc. These issues are fundamentally interesting and they are linked to technological applications. In the area of information storage, progress both benefits from and drives micromagnetic imaging research. This has been particularly true in the last few years, with a rapidly growing number of studies now focusing on controlling, manipulating [25,26], and moving the nano-scale internal magnetic configuration of domain walls [27,28]. These examples highlight the importance of combining nanometer-scale spatial resolution, sub-nanosecond temporal resolution, three-dimensional mapping of magnetization and element-specificity, by providing more detailed understanding of the correlation between structure and magnetism.

Only a few years after Telieps and Bauer published their first (non-polarized) low-energy electron microscope (LEEM) images [29,30], a team led by Poppa and Bauer outfitted the instrument with a spin-polarized electron source, allowing first demonstration of the principle of spin-polarized low-energy electron microscopy (SPLEEM) imaging of magnetic domain structures [31,32]. Soon after that, a versatile vector-magnetometric imaging

[a] e-mail: nicolas.rougemaille@grenoble.cnrs.fr

technique was achieved when Duden and Bauer developed a compact electron spin polarization manipulator [33], turning SPLEEM into a powerful tool for mapping spin-structure with very good spatial- and angular resolution. An additional compact LEEM instrument designed by Grzelakowski and Bauer [34] was also equipped with an electron spin polarization manipulator. Both these SPLEEM instruments are still in use today, the first was recently moved to Hong Kong University of Science and Technology and installed in the group of M. Altman, the second is being operated as a user-facility at the National Center for Electron Microscopy of the Lawrence Berkeley National Laboratory in California. In addition, a commercial SPLEEM instrument [35] was installed in the Solid State Physics group at the University of Twente, The Netherlands; and a new instrument was equipped with an advanced high-brightness spin-polarized source at the Osaka Electro-Communication University in Japan [36,37].

Goal of the present article is to review how application of SPLEEM can contribute to the field of magnetism at small scales. Complementing several excellent earlier reviews [38–40], this paper highlights recent advances. The diversity of the materials and phenomena that have been investigated by SPLEEM [31–88] underlines the maturity of the technique as a micromagnetic imaging tool, and the results also point to extensive opportunities for new applications. At this time scientific output remains limited by the number of available instruments and we anticipate that the field will benefit from the availability of new microscopes.

The basic principles of SPLEEM instrumentation are described in Section 2, with brief attention to common methods to produce spin-polarized electron beams, and a summary outlining the basic approach to forming images with magnetic contrast under such a beam. Advantages and limitations of the technique are also discussed to illustrate its complementarity with other magnetic imaging methods. Sections 3–5 are dedicated to examples for which SPLEEM has been used: to investigate spin reorientation transitions in Ni/Cu(001) ultrathin films and Fe nanowires self-organized on W(110) surfaces, to study micromagnetic configurations and bistability phenomena in Co dots grown on Ru(0001), and to explore magnetic couplings in ferromagnetic/antiferromagnetic/ferromagnetic layered structures, respectively. These different studies highlight how the combination of in situ and real time magnetic imaging give new insights into the physics of these systems. In Section 6 we review how SPLEEM also allows spectroscopic measurements, which can be a useful tool to probe spin-dependent unoccupied band structure of magnetic materials as well as electronic properties of buried magnetic interfaces. Finally, concluding remarks are given in Section 7.

2 SPLEEM microscopy: basics

In a SPLEEM microscope, spin-polarized, low-energy electrons are projected toward the sample surface through an illumination column. Just before reaching the surface, the electron beam is decelerated within a cathode lens and illuminates the surface in normal incidence (Fig. 1). The incoming electron beam and the backscattered electron beam are separated in a magnetic beam splitter. A magnified image of the surface is obtained by passing the backscattered beam through an imaging column, similar as in a conventional transmission electron microscope. The typical energy of the electron beam (at the specimen surface) is a few eV above the vacuum level. As a consequence of the low inelastic mean free path of ballistic electrons inside solids, the technique is extremely surface sensitive, and the properties of the top few atomic layers of the sample dominate image contrasts. In this sense, depth-resolution of SPLEEM is extremely high (atomic-scale). Lateral resolution is moderate, perhaps of the order of 10 nm in conventional instruments. It should be noted that with the development of aberration correction techniques [35,89–91], remarkable improvements of lateral resolution are becoming available in LEEM instruments and we can anticipate that resolution of the order of 2 nm will soon be possible in SPLEEM.

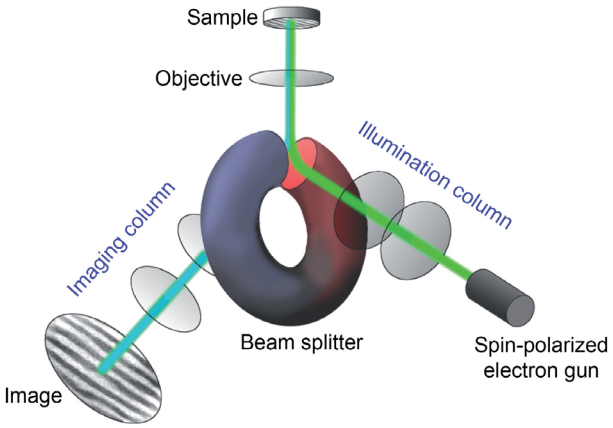

Fig. 1. (Color online) Schematics of a SPLEEM microscope. Spin-polarized electrons, photoemitted from a GaAs photocathode, are injected into a spin manipulator where azimuthal and polar orientation of the polarization is adjusted (see text for details). Then, the electron beam passes through an illumination column, before being decelerated in the objective lens. Electrons finally hit the surface with normal incidence. Electrons that are backscattered elastically are collected in an imaging column and focused on a phosphorous screen, where a magnified image of the surface is obtained. The incoming and reflected electron beams are separated in a magnetic beam splitter using the Lorentz force.

Employing a spin-polarized electron beam for illumination, the technique is also sensitive to the surface magnetization. In this section, we briefly recall three aspects of the technique: the working conditions of the spin-polarized electron gun, the origin of magnetic contrast, and the advantages and limitations of SPLEEM for magnetic imaging. For a more complete analysis of resolution and magnetic contrast, and for further details on the instrumentation, we refer the reader to other LEEM and SPLEEM review papers [38–40,92,93].

2.1 The spin gun

As in many other electron microscopes, the (unpolarized) electron source in a conventional LEEM is often a LaB_6 filament. SPLEEM, however, requires spin-polarized electrons, and the LaB_6 filament is replaced by a spin gun. The spin gun is composed of two main elements: the spin-polarized electron source that produces electron beams with a known spin polarization, and a spin manipulator, which allows accurate control of the spin polarization vector before the electron beam hits the sample surface.

Optical spin orientation in semiconductor photocathodes [94,95] is nowadays widely used for producing intense and highly polarized electron beams, and most spin-polarized electron sources rely on GaAs photocathodes (or strained GaAs-based heterostructures) under optical pumping conditions. In bulk-like, p^+-doped GaAs photocathodes under illumination with circularly-polarized near-bandgap laser light, electrons with up to 50% longitudinal spin polarization P_0 are excited in the bottom of the conduction band. This spin polarization can be switched from $+P_0$ to $-P_0$ by reversing the helicity of the laser light polarization. Since the bottom of the conduction band in the bulk material is typically 2.5 eV below the vacuum level for a clean GaAs surface, these polarized electrons are not emitted spontaneously into vacuum. Electron emission can be achieved by lowering the work function of the GaAs surface by coadsorption of cesium and oxygen in ultrahigh vacuum conditions (activation to negative electron affinity) [96]. The 50% polarization limit mentioned above is a consequence of the degeneracy of two different electronic bands at the valence band edge, with both bands contributing carriers during photoexcitation. The band degeneracy can be lifted by straining the crystal. When a strained GaAs crystal is illuminated with a precisely tuned laser, photoexcitation can be limited to involve carriers from only one of the valence bands; in principle this permits the excitation of 100% polarized carriers. In practice, spin-polarized electron sources based on strained GaAs heterostructures exhibiting spin polarization higher than 80% and quantum yield of about 0.1% have been demonstrated [97], and this type of sources can be used for SPLEEM [36,37]. For bulk-like, p^+-doped GaAs photocathodes and typical laser wavelength of approximately 800 nm, spin polarization is of the order of 25−30%. Such cathodes can be robust sources of quasi mono-kinetic spin-polarized electrons (the quantum yield can be as high as several percent, and the energy spread of the electron beam can be low, of the order of 100 meV).

To control the orientation of the polarization of the electron beam, a specially designed electron optics called spin manipulator is inserted between the GaAs photocathode and the illumination column. This electron optics combines electrostatic and magnetic deflectors to control the trajectory of the electron beam and the precession of its spin polarization. Spin manipulators used on SPLEEM instruments are described in more detail in references [33,36] and [64]. Figure 2 sketches the main features. Longitudinally spin-polarized electrons are injected into an electromagnetic deflection system which bends the trajectory of the beam by 90° (the element is similar to a Wien filter). Within this element, a vertical (along the z-axis in Fig. 2) static magnetic field is applied to rotate the spin polarization in the horizontal (x, y) plane. In a subsequent electron optical element (essentially a weak magnetic lens) a horizontal (along the x-axis) static magnetic field is used to rotate the polarization in the vertical (y, z) plane, without affecting the beam trajectory. Using this manipulator, the spin polarization of the incident electron beam can be precisely oriented in any spatial direction.

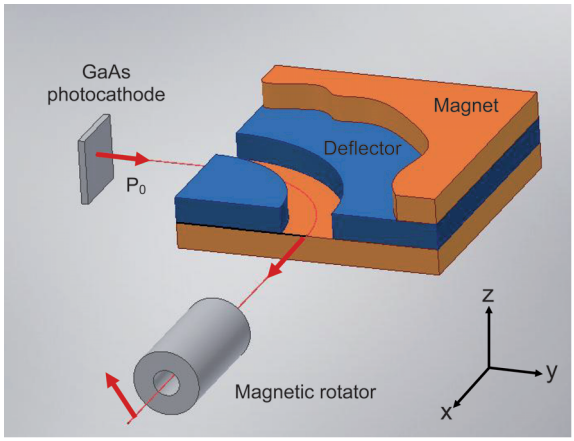

Fig. 2. (Color online) Schematics of the spin manipulator (reproduced from Ref. [64]). Longitudinally spin-polarized electrons are emitted by a GaAs photocathode under optical pumping conditions. These electrons are injected into a first set of electrostatic and magnetic elements (blue and orange elements, respectively), where the polar angle of the spin polarization is adjusted. Azimuthal orientation of the spin polarization is adjusted in a second electromagnetic element: this magnetic rotator is used to control the precession of the spin polarization around a horizontal, static magnetic field, parallel to the x-axis.

2.2 Origin of magnetic contrast

When a spin-polarized electron beam strikes a ferromagnetic surface, the number of electrons backscattered elastically from that surface depends, among other things, on the relative orientation of the spin polarization $\boldsymbol{P}_0$ of the incident electrons and the surface magnetization $\boldsymbol{M}$. In practice, $\boldsymbol{M}$ is unknown and $|\boldsymbol{P}_0|$ is modulated between $+P_0$ and $-P_0$ (see Sect. 2.1). The asymmetry $(I_+ - I_-)/(I_+ + I_-)$ of the corresponding reflected intensities I_+ and I_- gives the magnetic contrast, which is proportional to $\boldsymbol{P}_0 \cdot \boldsymbol{M}$. Conventional SPLEEM images are simply pixel by pixel representations of this reflection asymmetry. Relatively bright or dark features in the images result from relatively large values of the component of the surface magnetization vector along the axis defined by the orientation of the spin polarization of the illuminating beam. No magnetic contrast, i.e. 50% gray color in a SPLEEM image, is observed if $|\boldsymbol{M}| = 0$ (nonmagnetic surface) or if the spin polarization of the incident electron beam is perpendicular to the direction of magnetization in

a ferromagnetic surface. This latter point can be very useful when one is interested in good angular resolution in measuring magnetization direction: finding null-contrast as a function of varying the spin direction of the illuminating electron beam, rather than searching for maximal magnetic contrast, often provides greater angular sensitivity (an illustrating example is described below in Sect. 2.3 and Fig. 4).

Spin-dependent reflectivity of a ferromagnetic surface originates from two effects. First the elastic scattering potential between the spin-polarized incident electrons and the electrons in the ferromagnetic target is spin-dependent. In principle, both the spin-orbit and exchange interactions make the cross section in these electron-electron elastic collisions spin-dependent. However, under the conventional condition of normal incidence of the incoming and reflected electron beams, the spin-orbit interaction does not contribute to the intensity asymmetry. In good approximation, the exchange interaction often dominates SPLEEM magnetic contrast.

Inelastic electron-electron collisions also contribute to the SPLEEM contrast, because the inelastic mean free path (IMFP) of hot electrons is not only material dependent [98,99] but also spin-dependent in a ferromagnet [100,101]. Approximately, the IMFP is inversely proportional to the number of unoccupied s and d electronic states above Fermi energy in which a hot electron can "fall" (see Fig. 3a) [102]. Since the number of unoccupied states is larger for minority-spin electrons than for majority-spin electrons, minority electrons are more effectively scattered than majority electrons. Consequently, reflectivity of majority electrons is larger than the reflectivity of minority electrons. Note that in this simple description where spin exchange scattering is neglected, the scattering potential in electron-electron collisions does not need to be spin-dependent: only the Coulomb potential is taken into account in the calculation of the spin-dependence of the IMFP.

Both effects become less efficient as the energy of the incoming electrons increases. This is so because i) the exchange potential decreases rapidly with energy; and ii) the spin-dependence of the IMFP decreases when the electron kinetic energy becomes large compared to the exchange splitting in the density of states of the d bands (see Fig. 3a). For this reason, the best magnetic contrast in SPLEEM is usually obtained for low-energy electrons, with energy of a few eV.

One way to visualize the origin of SPLEEM magnetic contrast is to consider the spin-split band structure of ferromagnetic materials (see Fig. 3b). Ballistic electrons can penetrate into a crystal if unoccupied electronic states are available. If there is an energy-gap in the material for the wave vector of the injected electrons, then most of the incident beam will be elastically reflected (within a band-gap, electrons only penetrate into the crystal as evanescent waves). In a ferromagnet, due to the exchange interaction, bands are energy split for the two spin directions. In the energy range between the onsets of the majority- and minority-spin bands, electrons whose spin is parallel to the majority spins penetrate into the crystal, while electrons whose spin is parallel to the minority spins are reflected. This difference in reflectivity can lead to strong magnetic contrasts.

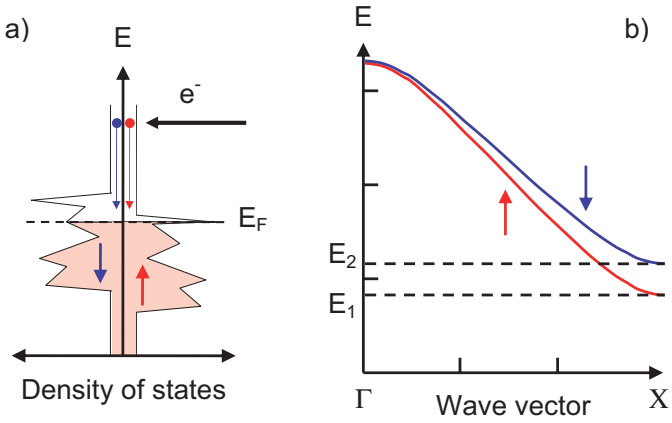

Fig. 3. (Color online) Two mechanisms leading to a different number of majority- and minority-spin electrons reflected from a ferromagnetic surface. (a) Density of states in a ferromagnetic metal. Due to the different number of unoccupied electron states above Fermi energy for the two spin directions, the inelastic mean free path between electron-electron collisions is larger for majority spins than for minority spins. (b) Sketch of the spin-split band structure in a ferromagnet along the (ΓX) crystal direction. For an incident beam of energy ranging from E_1 to E_2, majority-spin electrons enter the crystal, while minority-spin electrons are effectively reflected due to the lack of available states.

An additional contrast mechanism appears in very thin films where quantum well resonances can occur. In this case, the magnetic contrast can be enhanced, reduced or inverted due to Fabry-Pérot interferences in the quantum well [41,77–80]. Consequently, a given ferromagnetic surface can exhibit very different energy-dependencies of the magnetic contrast when the electron beam is injected into the surface of a bulk-like material or of an ultrathin film. This mechanism is illustrated in more detail in Section 6.

2.3 Advantages and limitations

Like in conventional LEEM microscopy, the surface sensitivity of SPLEEM is very high. This fact limits the usefulness of SPLEEM for studying samples that have been prepared elsewhere: with most materials, contaminants from exposure to atmosphere strongly affect what SPLEEM images show, and must be removed for imaging. To derive optimal advantage from the high surface sensitivity, it is most useful to equip SPLEEM instruments with a full suite of in situ surface preparation tools (sputtering and annealing procedures in well-controlled atmospheres) and film deposition sources (either in the microscope chamber or in other attached chambers). SPLEEMs are operated under good ultra-high vacuum conditions (base pressure in the low 10^{-11} Torr range), and it can be very useful to add complementary characterization capabilities on the same vacuum system, such as Auger

spectroscopy. Combined with other surface characterization techniques, SPLEEM allows quantitative analysis of structure-magnetic property relationships. Materials and structures can be grown or annealed in situ, while imaging. One might look at the instrument as a molecular beam epitaxy sample preparation system first, and consider the SPLEEM optics a monitoring instrument: this perspective highlights the strengths of SPLEEM for in situ micromagnetism research.

As a diffraction experiment, SPLEEM works well with crystalline samples. Non-crystalline or polycrystalline surfaces can be more problematic, because in this case the distribution of backscattered electrons over a wide angular range can lead to very low image intensity. With single-crystal samples, the high intensity of the specular beam often permits imaging at relatively high frame rates. LEEM images with useful signal-to-noise quality can be collected at video rate. Magnetic contrast is often weaker than other surface-structure contrast, which is why pixel by pixel difference images taken with two opposite spin polarizations are usually formed; in practice acquisition time for SPLEEM with good signal-to-noise quality is of the order of 1 s (of course optimal image integration time can strongly depend on sample material and many other factors). As we review in later sections, typical SPLEEM image acquisition time is very suitable to study in real time dynamical magnetic phenomena, such as spin reorientation transitions.

SPLEEM images are two-dimensional, but magnetization is a vector with three components. Of course the three-dimensional nature of magnetization is at the basis of the richness of micromagnetic phenomena and it can be interesting to map all components of the magnetization vector. This can be done by measuring image contrast in several SPLEEM images of the same surface area. For example, one can align the spin manipulator in three different settings, with spin polarization of the electron illumination aligned along either of two orthogonal directions parallel to the sample surface, or in the direction along the surface normal. Comparing magnetic contrast in triplets of SPLEEM images acquired with the three orthogonal settings of the spin manipulator then permits determination of the sample magnetization vector with good spatial resolution and good angular resolution. This type of approach can be used to understand the internal structure of domain walls or other more complex magnetization patterns. Angular resolution can be quite good, for example Figure 4a–4c shows SPLEEM images of a 3 nm-thick Fe/W(110) film where the orientation of local magnetization is precisely measured and the internal magnetic configuration of a 180° domain wall resolved. Note that a 1° variation of the incoming spin polarization results in a detectable change in magnetic contrast (see intensity profiles reported in Figs. 4d, 4e). This advantage of SPLEEM was used in the work reviewed in Sections 3 and 4.

Although SPLEEM is a surface sensitive technique, magnetic domain imaging of buried ferromagnetic films or interfaces is sometimes feasible. SPLEEM measurements on nonmagnetic (metal or oxide) thin layers deposited in situ on top of ferromagnetic films can sometimes reveal the domain microstructure of the underlying magnetic material (see Sect. 6). In some cases, the magnetic domains in such capped ferromagnetic films can still be imaged after exposure of the sample to air [76]. These results illustrate the versatility of SPLEEM, pointing to possible techniques for studing ex situ prepared crystalline samples.

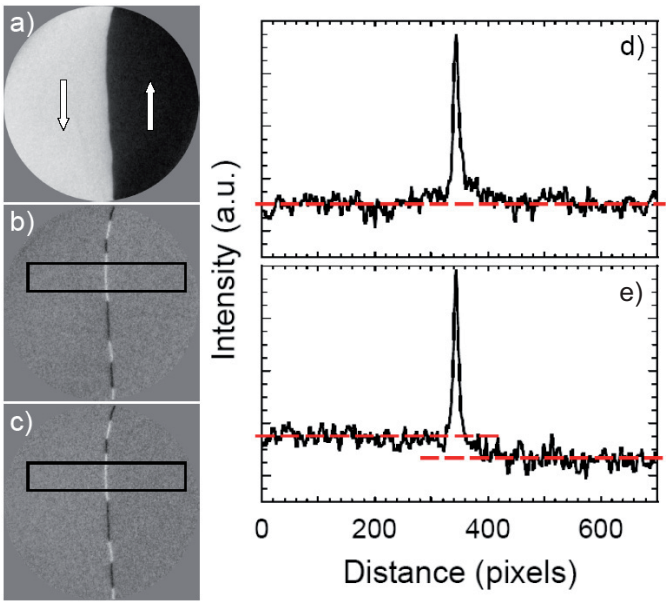

Fig. 4. (Color online) Magnetic domains and domain walls in a 3 nm-thick Fe film grown on a W(110) single crystal. Field of view is 5 μm. (a) The spin polarization of the incident electron beam is aligned along the direction of magnetization (white arrows) in the Fe film ([1–10] direction). (b, c) The incident spin polarization is rotated by 90° and 89° respectively to spatially resolve the internal chirality of the 180° domain wall. (d, e) Intensity profiles across the 180° domain wall, averaged within the black frames shown in (b, c). Although no obvious contrast is observed in (b, c) between the two magnetic domains, intensity profile reported in (e) clearly reveals their orientation, demonstrating in that example that sensitivity to the local direction of magnetization is better than 1°.

The spin-polarized electron beam propagating along the optical axis makes it challenging to image with an applied magnetic field. Even moderate-strength magnetic fields applied within the surface plane would deflect the electron beam too much for imaging. However, it is possible to apply magnetic fields in the surface-normal direction while imaging. This geometry minimizes deflection of the electron beam. An example of a magnetization reversal experiment can be found in reference [71], where a hysteresis loop of perpendicularly magnetized Fe/Cu(100) films is deduced from SPLEEM images.

In the following sections, several examples will be reviewed to show how the combination of in situ and real time 3D mapping of local magnetization makes SPLEEM a useful tool to reveal new insights into the physics of spin reorientation transition phenomena, micromagnetic configurations in low-dimensional structures or magnetic couplings in multilayers.

3 Spin reorientation transitions

In low-dimensional ferromagnetic systems, the direction of spontaneous magnetization generally results from the interplay between magnetocrystalline, magnetoelastic and shape anisotropies. The balance between these anisotropies can vary, particularly in magnetic films and layered structures, when temperature, sample thickness, or surface composition is changed. These effects often result in reorientations of the magnetization. Because any change of magnetic domain microstructure in a material can be studied in situ and in real time, SPLEEM is a powerful tool to investigate spin reorientation transitions (SRT) in low-dimensional structures. The direction of the magnetization vector can be mapped with high angular- and spatial resolution while the spin transition occurs, for instance when the thickness of the structure is increased, when the temperature is changed, or when the surface topography, morphology or chemistry is modified. Co on Au(111) [54], Co on Ru(0001) [61] and Co/Ru(0001) with noble-metal capping layers [62], Au/Co on Ru(0001) [54] and on W(110) [53,59], Fe on Cu(001) [67], Fe/Ni bilayers on Cu(001) [73] and Fe-Co alloys on Au(111) [82] are examples of systems exhibiting SRTs that have been investigated using SPLEEM. The capabilities of SPLEEM make it a complementary approach to other techniques, but also open new opportunities for magnetic investigations. In this section, we review two studies where SPLEEM was used to investigate SRT phenomena in magnetic thin films.

3.1 Ni on Cu(001)

Thickness-dependent SRTs from out-of-plane to in-plane magnetization often occur in ferromagnetic thin films. At low thicknesses, surface effects dominate and give rise to large, perpendicular magnetocrystalline anisotropy, while for thicker deposit dipolar shape anisotropy forces the magnetization to lie in the film plane. Co ultrathin films grown on Au(111) are one well-known system showing such a SRT when the film becomes thicker than 4–5 monolayers [103,104].

Ni thin films epitaxially grown on Cu(001) also show a magnetization reorientation transition. It is of particular interest because an unusual, inverse SRT from in-plane to out-of-plane is observed when the thickness of the Ni film is increased. This unexpected SRT has stimulated a large number of experimental and theoretical studies, and the atomic structure of Ni/Cu(001) films has been shown to play a key role. In fact, due to a small lattice mismatch (about 2.5%) between the two materials, pseudomorphic Ni films can be grown on Cu(001) single crystals up to a thickness of 11 monolayers [105]. The strained Ni crystal structure in these films causes a negative magnetocrystalline surface anisotropy that favors in-plane magnetization, and a positive volume anisotropy favoring out-of-plane magnetization [106]. Since the dipolar shape anisotropy is smaller than the volume anisotropy in these films, the SRT proceeds from in-plane to out-of-plane. Although this system is now quite well understood, there remain questions whether the SRT proceeds via a discontinuous (first order transition) or a continuous (second order transition) rotation of the magnetization [107–110]. SPLEEM was used to address this issue, taking advantage of the possibility to map the magnetization vector in real time as the SRT occurs during film deposition.

SPLEEM results show that the SRT is surprisingly complex and there is no simple answer as to whether the kinetics of the SRT phase transition is of first- or second order [65]. Consider Figure 5, reproducing maps of the surface magnetization vector of a Ni thin film during growth on a stepped Cu(001) single crystal with a 2° miscut in the [011] direction. Three orthogonal components of the magnetization have been probed: one out-of-plane component (normal to the surface) and two in-plane components, parallel and perpendicular to the mean direction of the Cu atomic steps, which was determined from LEEM images (not shown here). At 7.68 ML Ni film thickness, the dark color of the upper left panel in Figure 5 indicates that the value of the in-plane component of the magnetization vector following the substrate step direction is large, while the absence of bright or dark color in the two panels below shows that the in-plane component orthogonal to the substrate steps and the out-of-plane component are both small: i.e., before the SRT, the magnetization lies in the film plane and is aligned along the Cu atomic steps. Around 8 Ni monolayers thickness, the dark color of images in the middle row indicates that magnetization abruptly rotates within the film plane, into the direction perpendicular to the steps. This rotation takes place via nucleation and growth of domains (see 8.00 ML and 8.08 ML panels), suggesting first order kinetics. At slightly higher film thickness (for example up to 8.24 ML) magnetic contrast is visible for all three probed components of magnetization. The magnetization vector is in a canted state with respect to the surface normal, and the in-plane component of the magnetization vector is rotated by about 70° with respect to the atomic steps of the Cu substrate. As more Ni is deposited, the progressively evolving contrast in the SPLEEM images reveals that the magnetization continuously rotates towards the out-of-plane direction. In the last column of images (9.36 ML Ni thickness) the bright color of the bottom right image, together with absence of bright or dark color in the corresponding in-plane images, indicate that the SRT is complete and the magnetization vector is now perpendicular to the surface. The relatively wide range of thickness where the SRT occurs suggests that the kinetics of the rotation of the surface magnetization from in-plane to out-of-plane is of second order. SPLEEM thus reveals that the SRT in stepped Ni/Cu(001) films proceeds via a discontinuous rotation of the in-plane component of the magnetization from parallel to roughly perpendicular to the substrate atomic steps, followed by a continuous rotation of the magnetization from in-plane to out-of-plane.

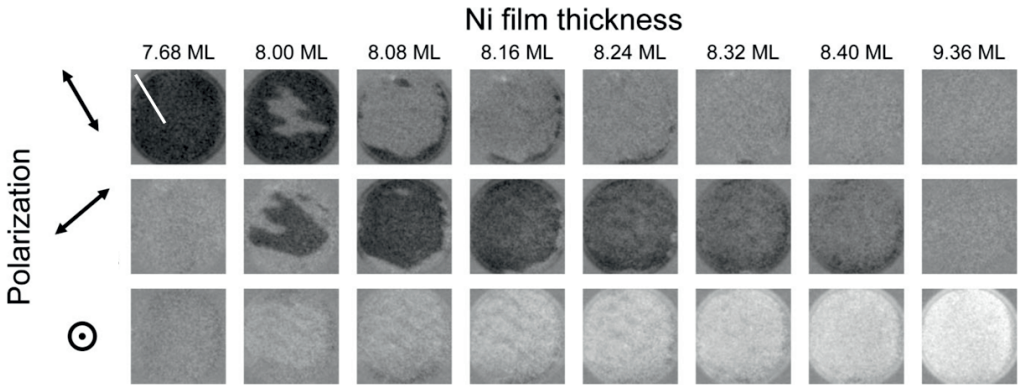

Fig. 5. From reference [65] with permission. In situ SPLEEM observation of the thickness-dependent spin reorientation transition that occurs when Ni thin films are grown on a stepped Cu(001) single crystal. Incident spin polarization direction is indicated by black arrows. For Ni deposits thinner than about 7.7 monolayers, the surface magnetization lies within the film plane, parallel to the Cu atomic steps (white line in upper left SPLEEM image). For thicker deposits, nucleation and growth of magnetic domains with a canted magnetization is observed (see evolution of both in-plane and out-of-plane components). For a Ni thickness of about 9.4 ML, the Ni film is completely magnetized perpendicular to the surface. Field of view is 7 μm.

These results show an influence of the substrate step structure on the direction of magnetization during the SRT and raise the question whether the kinetic order of the SRT might be changed by changing the atomic step morphology of the Cu surface. In reference [66], the capability of SPLEEM to prepare and characterize in situ the Cu(001) substrate, together with the possibility to map the magnetization vector during Ni deposition, were used to investigate this issue. Controlled Ar ion bombardment cycles combined with careful annealing schedules result in the promotion or suppression of step-bunching on the Cu(001) single-crystal. Thus, one can tune the local step density of the Cu(001) surface prior to Ni deposition. Image sequences similar to the one reproduced in Figure 5, but obtained for different substrate step morphologies, show that second-order SRTs are observed when atomic step-bunches are suppressed (not shown here; see Ref. [66]), while first-order transitions are found for step-bunched Cu surfaces. These results suggest that the atomic step structure of the Cu(001) single crystal influences the kinetic order of the in-plane to out-of-plane SRT. Dependence of magnetic anisotropy contributions on substrate topography must be taken into account to describe the SRT in Ni/Cu(001) thin films. For this purpose, the magnetization-dependent, anisotropic part of the free-energy density f can be written [66]:

$$f \approx -K_2 \cos^2\theta - \frac{1}{8} K_4 \left(3 + \cos 4\varphi\right) \sin^4\theta. \qquad (1)$$

In equation (1), K_2 and K_4 are the second-order and fourth-order anisotropy constants, while θ and φ are the angles between the magnetization vector and, respectively, the surface normal and the [001] direction [111]. To visualize the relative weight of K_2 and K_4 in the SRT, it is convenient to plot the K_2–K_4 phase diagram corresponding to the minimization of the free energy density f. The thickness dependence of K_2 and K_4 is shown in Figure 6, using the values found in reference [106]. The phase diagram can be divided into four regions; three stable regions, where the magnetization is purely out-of-plane (vertical-hatched), purely in-plane (horizontal-hatched), in a canted state (not hatched), and a metastable region (cross-hatched) separating the first two stable regions. The plot shows that when the Ni film thickness is in the range 7.3 ML $< d <$ 7.8 ML, the K_4 vs. K_2 curve crosses the un-hatched region where the magnetization is in a canted state, and the transition is of second order. A first-order transition would be expected when the K_4 vs. K_2 curve crosses the cross-hatched metastable region. For this, the K_4 vs. K_2 curve would have to shift either towards the right (larger value of K_2) or upwards (larger value of K_4). Increasing K_2 to the point where a first order transition results would imply that the critical thickness of the SRT decreases by more than 1 ML. Although surface roughness or adsorbates are known to change the critical thickness for which SRTs occur, such a change was not observed in these SPLEEM experiments. On the other hand, even a moderate increase of the fourth-order anisotropy constant can shift the phase diagram into the coexistence region, and previous work [112] has already pointed out the effects of inhomogeneities at interfaces on the K_4 constant. To illustrate the impact of step-bunches (inhomogeneities), a +15 μeV/atom was added to the K_4 value from reference [106], and the minimization of the free-energy density was recompiled to obtain the phase diagram. The results plotted in Figure 6 using triangular symbols show that this plausible change is sufficient to avoid the stable region where magnetization is in a canted state, and thus can explain the observation of an abrupt transition from in-plane magnetized Ni films to an out-of-plane configuration (first order transition) for the case of step-bunching on the Cu(001) substrate surface.

In summary, a careful preparation of the Cu(001) surface atomic step structure allows the control of the SRT kinetic order. The density of atomic steps on the Cu substrate is found to be the crucial parameter to

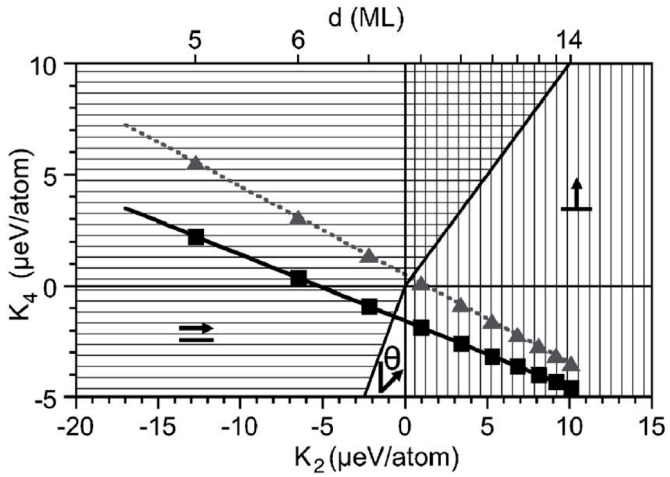

Fig. 6. From reference [66] with permission. K_4 vs. K_2 phase diagram for Ni/Cu(001) films deduced from the minimization of f (see Eq. (1)). Three stable regions are observed where magnetization is purely in-plane (horizontal hatched), out-of-plane (vertical hatched), or in a canted stated (no hatch). A metastable region (cross-hatched) separates the two regions where magnetization is purely in-plane and out-of-plane. Square symbols are obtained from values given in reference [106]: in-plane to out-of-plane SRT occurs via the canted state, and transition is of second order. If these K_4 values are increased by 15 μeV/atom to account for substrate topography effects, then the SRT crosses the metastable region, and transition is of first order.

observe either first order or second order SRT, thus reconciling discrepancies between reports in previous literature [107–110]. Beyond the interpretation of SRTs in Ni/Cu(001) films, this work illustrates the strength of combining, in situ and in real time, topography and structural information with accurate 3D mapping of the local magnetization distribution to reveal phenomena that would have been invisible otherwise.

3.2 Self-organized Fe wires on W(110)

An in-plane SRT also occurs in epitaxial, nanometer-thick Fe films grown at room temperature on W(110) surfaces. Fe films become magnetic at a thickness of about 1.5 ML [113] with an easy axis of magnetization parallel to the [1–10] direction, due to a strong surface anisotropy. This magnetization axis remains stable up to about 50 ML thickness [114], above which a SRT occurs and the [001] direction becomes the new easy axis of magnetization (i.e. the magnetization rotates 90° within the surface plane), as expected for bulk Fe. This SRT is also observed for thinner deposits, when room temperature grown Fe films are subsequently annealed a few minutes at several hundred K [115,116]. However, in that case, the SRT is accompanied with the dewetting of the Fe film and the formation of islands elongated along the [001] direction. Different factors have been suggested as the driving mechanism for this SRT: reduction of magnetoelastic anisotropy (stress relief during the annealing procedure), strong shape anisotropy of the elongated islands, or reduction of surface anisotropy (due to the change in the film morphology, islands are much thicker than the nominal thickness of the as-grown Fe film) [115]. In this context, a key question is: what influence has the dewetting dynamics on the SRT? For this type of problem, SPLEEM is ideally suited to obtain spatially resolved magnetic information in real time, during morphological changes that occur while annealing. For the Fe/W(110) system, SPLEEM measurements added new insights into the origin of this SRT [74,84].

Results are summarized in Figure 7 for a 14 monolayer-thick Fe film grown on a W(110) single crystal exhibiting pronounced step-bunching (see LEEM image in Fig. 7a). The surface topography in an early stage of the dewetting process is shown in Figure 7b. Dark regions are places where the Fe film had already dewetted. Dewetted zones are often found to nucleate at step-bunches and to extend roughly along the [001] direction, forming very long, parallel grooves in the Fe film, as observed in Cr/W(110) thin films [117]. As the annealing proceeds, Fe removed from the grooves accumulates on the remaining Fe ribbons, increasing locally the film thickness. The corresponding magnetic images for a spin polarization of the incident electron beam along the [1–10] and [001] directions are given in Figures 7c and 7d, respectively. Away from the dewetted regions, magnetization lies along the [1–10] direction (large black magnetic domain), as observed for continuous films before annealing (see Fig. 4). Note that no magnetic contrast is found in the voids (Fig. 7c), since only one atomic wetting layer, which is not ferromagnetic at room temperature, remains on the W surface [118]. However, a local in-plane canting of magnetization is observed in the regions adjacent to the voids (see black and white magnetic contrast around the voids in Fig. 7d). Evidently the SRT starts at the same time as the Fe film starts to dewet and concludes with the formation of the Fe islands (Fig. 7e). These observations support the notion that magnetoelastic effects are not the key driving force for the reorientation of magnetization, and highlight the role of the dewetting dynamics on the SRT mechanism [74]. With increasing annealing time, SPLEEM measurements show that the canted magnetization around the voids provides a bias to initiate the magnetization reorientation. Mapping the surface magnetization reveals that it follows the edges of the voids, and is not necessarily oriented exactly along the [001] crystal axis. In other words, while the magnetization of the continuous films is aligned along the [1–10] direction of the W substrate, the direction of magnetization in the elongated Fe islands may or may not be aligned along the [001] direction, depending on how these islands are oriented after the annealing is complete. Reduction of surface anisotropy does not appear to be a key driving force in the observed SRT. Rather, dipolar forces associated with the shapes of the voids that form when the film starts to dewet appear to initiate the rotation of magnetization while annealing, and ultimately the shape anisotropy of the islands determines the final easy axis of magnetization, as pointed out in other work [84].

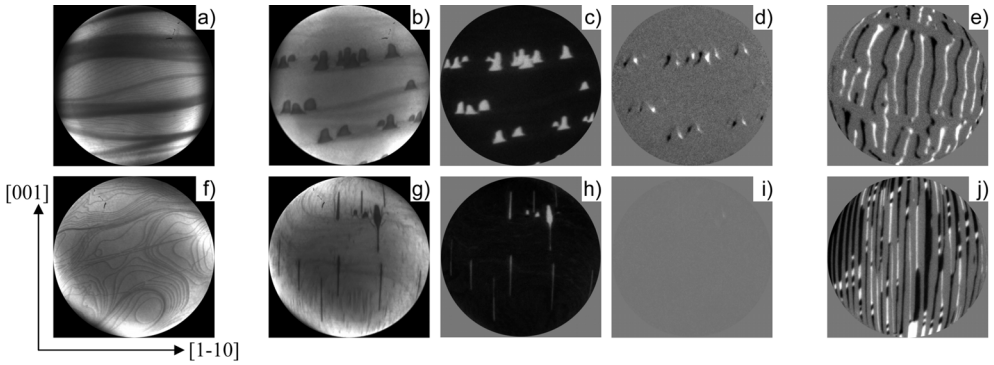

Fig. 7. From reference [74] with permission. In-plane spin reorientation transition in annealed Fe films grown at room temperature on two different W(110) single crystals. (a, f) Topographic image (LEEM mode) of the stepped and atomically flat W crystals (see text for details) prior to Fe deposition. (b, g) Topographic images of the surface upon annealing at about 600 K a 14 ML-thick Fe film deposited on these two W single crystals. Dewetted regions appear dark. The corresponding magnetic images for a spin polarization along the [1–10] and [001] are shown in (c, d) and (h, i), respectively. The shape of the dewetted regions depends on the substrate step structure and affects the magnetization distribution of the continuous film. (e, j) Complete annealing leads to the formation of a self-organized array of Fe wires. Field of view is 7 μm.

The influence of the void geometry on the canting of magnetization can be tested by initiating the dewetting process on surfaces with different step/terrace morphologies. One can compare substrate regions where atomically flat terraces are separated by step-bunches composed of multiple atomic-height steps, versus substrate regions where terraces are separated by single monolayer height steps. Indeed, under otherwise very similar experimental conditions, the SRT occurs via different mechanism in these two cases. When the W substrate does not show step-bunching (see Fig. 7f), voids appear at random locations on the surface (preferential nucleation sites where the film could start to dewet can not be identify with LEEM) and grow along the [001] direction (Fig. 7g). Here, voids have a pronounced rectangular shape and often proceed to grow at both their extremities. Contrary to what is observed during dewetting that is initiated at step-bunches (Fig. 7d), no magnetic contrast is detected along the edges of the grooves, and the magnetization of the continuous film remains aligned along the [1–10] direction (Figs. 7h and 7i). With further annealing, more grooves form and the width of the Fe ribbons trapped between them progressively shrinks. When the ribbon-width decreases below approximately 150 nm, shape anisotropy dominates over magnetocrystalline anisotropy, and the magnetization of the ribbons flips into the [001] direction. During dewetting at step-bunches on the W(110) substrate, voids often provide a bias for the canting direction of the magnetization. Here, the magnetization reorientation is often accompanied with the transient formation of a multidomain magnetic microstructure (Fig. 7j). Figure 8 shows a ribbon for which the SRT has taken place. From the topographic LEEM image the width of the wire is estimated to be about 200 nm. In Figures 8b−8d, bright and dark contrasts indicate the component of the magnetization along the orthogonal in-plane directions [1–10] and [001], and along the in-plane direction at 45 degrees between [1–10] and [001], respectively. On the upper and lower parts of the wire, magnetization has already rotated 90° and is aligned along the long axis of the Fe ribbon. However, the middle region of the ribbon exhibits flux-closure domain patterns. The local direction of magnetization within these domains, as deduced from the three SPLEEM images, is sketched in Figure 8e.

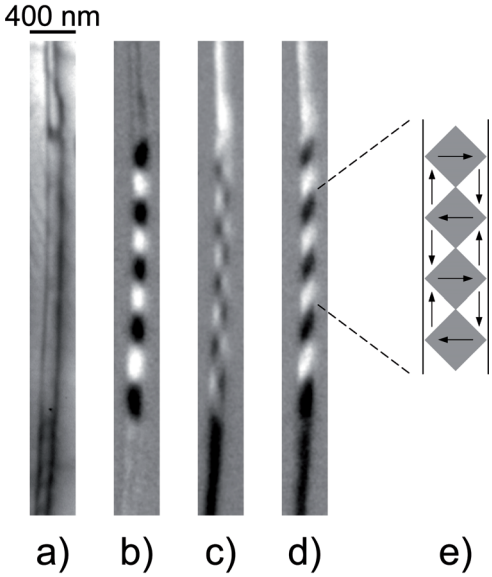

Fig. 8. From reference [74] with permission. (a) LEEM image of a Fe ribbon formed by annealing a 14 ML-thick Fe film grown at room temperature on an atomically flat W(110) surface (see text for details). Corresponding magnetic images when one probes the components of magnetization along the orthogonal in-plane directions [1–10] (b) and [001] (c) and, in panel (d), along the in-plane direction at 45 degrees between [1–10] and [001] (out-of-plane SPLEEM images, not reproduced here, show null-contrast). (e) Sketch of the magnetization distribution in the ribbon as deduced from the three SPLEEM images.

In summary, ribbon-shaped Fe islands that nucleated at substrate step-bunches are magnetized along their long axis, while Fe ribbons that nucleated within atomically flat substrates tend to exhibit flux-closure magnetic domain patterns. These results show how the relative importance of different magnetic anisotropy energies contributing to the SRT observed in Fe/W(110) films can be influenced by carefully tuned annealing schedules and by the choice of the substrate atomic step structure. Complementing information on island morphologies and magnetic properties of annealed Fe/W(110) films available from prior studies [119,120], the capability of SPLEEM to directly correlate, on the basis of real time in situ observations, surface morphology and local distribution of magnetization, has provided crucial insights into these SRT mechanisms.

4 Micromagnetic configurations of low-dimensional systems

Besides SPLEEM investigations of SRT phenomena, easy control of the incident spin polarization in all spatial directions allows one to map conveniently and accurately unknown micromagnetic configurations of small magnetic elements. As illustrated in Section 3, these magnetic configurations are governed by competition between several anisotropy energies. Below a critical dimension, elements are usually in a magnetic single-domain (SD) state, i.e. the magnetization is uniform across an element. As the size of elements increases, magnetostatic energy accumulates in the system until the magnetic single-domain state becomes unstable and breaks up into a multidomain configuration to minimize magnetic charges at the boundaries [26,86]. In highly symmetric objects, a vortex (V) state might be preferred compared to a multidomain configuration. This is sometimes the case for instance in disk-shaped magnetic elements. In the V state the in-plane magnetization curls around a central core while, at the vortex core, magnetization turns into the surface normal.

Micromagnetic computations can often predict the magnetic ground state of small elements and comparison of theoretical predictions with experimental images can reveal interesting effects. For example, for dots falling into a certain size range, micromagnetic calculations predict that the V state should be the ground state. In contrast, SPLEEM observations of as-grown Co nanodots have shown that SD states persist over a surprisingly large size range. This surprising observation can be understood by combining micromagnetic simulations with in situ measurements exploring the stability of magnetic domain configurations with respect to thermal activation. Based on the results, a new extended phase diagram with magnetic bistability of V and SD states near the phase boundary was proposed [50].

Co dots were epitaxially grown on a Ru(0001) surface, in the microscope chamber, and their aspect ratios were controlled by adjusting the deposition temperature and Co dose [50]. Co dots with a wide range of lateral dimensions (20−800 nm) and thicknesses (1–4 nm) were studied.

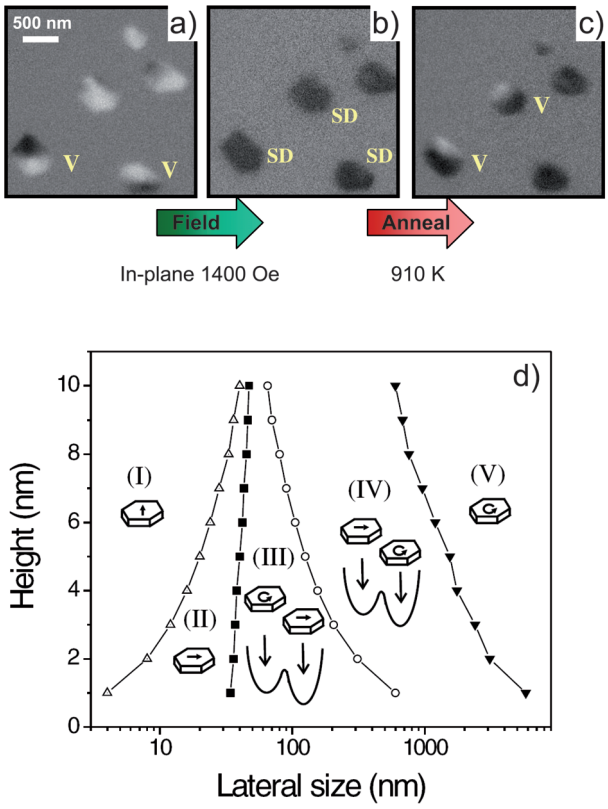

Fig. 9. (Color online) (a–c) Courtesy of Ding, Argonne National Laboratory, (unpublished) [121]. SPLEEM images of five Co nanodots on a Ru(0001) surface, showing bistable magnetization states. (a) On four of the dots, simultaneous presence of bright and dark regions indicates non-uniform magnetization states: the contrast variation on the two dots near the lower edge of panel (a), labeled V, is indicative of magnetic vortex states. (b) After application of a magnetic field (1400 Oe, parallel to the sample surface) the dark and homogeneous color of all five nanodots indicates that they have remained magnetized in single-domain states. (c) After briefly heating to 910 K, several of the nanodots are again in magnetic vortex states (labeled V). (d) From reference [50] with permission. Computed phase diagram showing the magnetic ground state configuration of Co nanodots as a function of height and lateral size. Regions (III) and (IV) illustrate the magnetic bistability of these dots in a wide range of size (see text for details).

Figure 9 shows SPLEEM images of an ensemble of five such Co dots with sizes in the neighborhood of 500 nm. These images show how individual nanodots in this size range can be switched from V states to SD states by application of external magnetic field pulses (Figs. 9a, 9b). Conversely, the dots can often be switched from SD to V states by thermal activation (Figs. 9b, 9c) [121].

To understand this metastability, the 3D solver of the OOMMF code [122] was used to compute the energy of magnetic states as a function of nanodot dimensions. In these simulations, Co dots were modeled as hexagonal prisms to simulate the shapes of the experimentally observed elements. Parameters used for the calculations are those of bulk hcp Co: exchange constant is set to

2.5×10^{-11} J/m, magnetization at saturation is chosen to be 1.4×10^6 A/m, and the dots are assumed to have uniaxial anisotropy along the *c*-axis with a constant equal to 5.3×10^5 J/m^3. In the computation, cell size is $2 \times 2 \times 1$ nm^3, which is much smaller than the exchange length in Co (about 16 nm). Interactions between dots were neglected, i.e. distance between dots is assumed to be large enough so that influence of dipolar interaction does not significantly modify the equilibrium magnetic domain configuration.

The equilibrium boundary between the SD and V states was estimated by computing the total energy of SD and V states for different heights and lateral sizes. Height and lateral size were varied from 1 to 10 nm and from 4 to 6000 nm, respectively. Results are shown in Figure 9d as open circles. It is also noted that for small lateral dimensions, particularly for thick dots, a spin reorientation transition (open triangles boundary) from perpendicular to SD in-plane configuration is found.

To explore possible bistability, nanodots were set in the energetically un-favored states (SD or V on the right side or on the left side of the equilibrium boundary (open circles), respectively) and were then allowed to relax. If the initial and the relaxed magnetic configurations are found to be the same, then the nanodot geometry is still in the bistability region, while it is out of the bistability zone when the relaxed magnetic configuration is different from the initial state. In Figure 9d, the solid square symbols boundary gives the lower limit where the V state can be stabilized, and the solid triangle symbols boundary gives the upper limit where the SD state can exist. Interestingly, this phase diagram shows broad bistability regions where V and SD states can both be stable (regions III and IV in Fig. 9d): transition from one state to the other requires the crossing of an energy barrier. For example, a 4 nm thick Co dot can be found either in the V state or the SD state for lateral sizes ranging from ∼40 nm to ∼1600 nm.

Thus, the initial observation that in freshly grown ensembles of Co nanodots SD states are very commonly observed and V states only very rarely can be understood as a consequence of sample history. In an early phase of their growth, the Co dots are so thin and small that the stable magnetic configuration is the SD state (region II in Fig. 9d). As deposition continues, the Co dots grow in size and thicken, but remain in the SD state throughout the bistability region. This picture explains the experimental observation that the as-grown dots tend to be in a SD state, even for dimensions that favor the V configuration as the ground state.

The authors of reference [50] computed the height of the transition barrier between SD and V states using an analytical model, and used SPLEEM to test whether observations of thermally activated transitions across this barrier are consistent with this theory. Indeed, transitions are observed after flashing the sample to 910 K. The observations of thermally activated transitions from SD to V states for a few nm-thick Co dot with typical 500 nm lateral dimensions are consistent with the calculated energy barrier and with the phase diagram (bistability region IV in Fig. 9d). This work demonstrates how the capability to prepare, characterize and image magnetic structures during deposition or annealing procedures, without losing the region of interest, makes SPLEEM a powerful tool for micro- and nano-magnetism.

5 Magnetic coupling in layered structures

Some spintronics devices, such as magneto-resistive sensors, hard disks read heads or non-volatile memories, require structures composed of ferromagnetic thin layers separated by nonmagnetic spacers [123]. In these systems, one ferromagnetic layer is made magnetically "hard" to reverse, while the second one, the "soft" layer, has a smaller coercive field so that its magnetization can be reversed, leaving the magnetic state of the "hard" layer unchanged. That way, the magnetic configuration in the overall structure can be prepared in two magnetic states (one magnetic bit) depending on the alignment (parallel or antiparallel) of the two magnetizations. Magnetic couplings may appear between the ferromagnetic layers, and understanding their origin is particularly interesting for spintronics applications, as well as for fundamental reasons. Magnetic imaging of layered systems can provide crucial information that may not be accessible otherwise. For example, magnetic stray fields generated by domain walls in the hard layer of a tunnel junction can significantly reduce the energy barrier to nucleate domains in the soft layer during magnetization reversal [124]. In micron-sized, ellipse-shaped spin valve structures, the magnetic stray field of the hard layer is also known to induce 360° domain walls in the soft layer [125].

Due to its small sampling depth, SPLEEM is not ideal for imaging separately the micromagnetic domain configuration of several nanometer-thick layers in a sandwich system; X-ray photo-emission electron microscopy (X-PEEM) is a better tool for such measurements. In that respect, X-PEEM offers more flexibility, especially to image ex situ prepared samples. However, the capability of SPLEEM (like X-PEEM) to image magnetic surfaces in situ allows one to study magnetic layers in a stack sequentially, during sample preparation. This was done for example in Co/Au/Co and Co/Cu/Co multilayers deposited on W(110) single crystals to study interlayer exchange coupling [57,58]. While X-PEEM microscopy also allows in situ magnetic imaging, the high surface sensitivity of SPLEEM can be beneficial, particularly when the two ferromagnetic electrodes are of the same chemical element (studying multilayer stacks, X-PEEM permits imaging of two ferromagnetic layers separately if they are composed of different elements. If the magnetic layers are made of the same element, then X-PEEM imaging may show superpositions of the domain structures of the layers).

Magnetic coupling also occurs at interfaces between ferromagnetic and antiferromagnetic materials. One important application of this type of coupling is the "exchange biasing" effect, which can be used to stabilize the magnetization of "hard" magnetic layers in spintronics devices. Understanding and measuring the

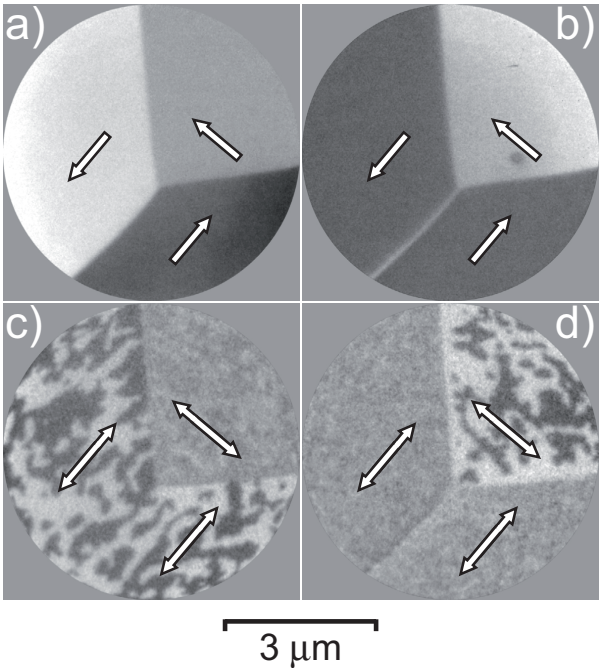

Fig. 10. SPLEEM images in panels (a, b) show magnetic domains in the first Fe electrode for two orthogonal spin polarizations of the incident electron beam. Large domains are magnetized along either [010] or [100] easy axes (local magnetization is represented by a white arrow), and width of the observed 180° domain wall is $\delta \sim 200$ nm. Panels (c, d) show images of magnetic domain structures in the top Fe-layer after completion of the Fe/NiO/Fe(001) trilayer structure. Delicate Ising-like domain structures include very small "bubble"- and "channel"-domains with widths as small as 70 nm. Domain wall width is below resolution of these images.

strength of the exchange interaction across ferromagnetic/antiferromagnetic interfaces is important, and microscopy is a useful tool in this field.

In ferromagnetic / antiferromagnetic / ferromagnetic sandwiches, the capability to image magnetic layers in a stack sequentially, and in situ during growth, has provided new insights into the origins of an unusual magnetic domain structure [75]. In this work, Fe/NiO/Fe(bulk) trilayers were grown on MgO(001) single crystals. First, a thick (300 nm typically) Fe film is grown on the MgO(001) crystal. Then, a 4 nanometer-thick NiO film is prepared by electron beam evaporation of pure Ni under an oxygen pressure of about 7×10^{-7} Torr, following a well established procedure [126]. Finally, the Fe top layer is deposited (film thickness in the 0−6 nm range) onto the freshly grown NiO film. As confirmed by low-energy electron diffraction (LEED), these structures are epitaxial with the [100] direction of the NiO lattice parallel to the [110] direction of the Fe lattice (45° orientation of the two cubic cells). Being grown at room temperature and under conditions of very low magnetic stray fields, these multilayers do not show macroscopic exchange bias.

The bulk-like Fe layer has macroscopic magnetic domains, with in-plane magnetization aligned either along the [010] or [100] crystal directions, due to the fourfold symmetry of the system (Figs. 10a, 10b). Domain walls are straight and run along the [100]- or [110]-type directions. The domain wall width observed in SPLEEM images, $\delta \sim 200$ nm (see Fig. 10b), is consistent with what one would expect from a textbook picture [1]: usually, wall width is proportional to the square root of the exchange/anisotropy energy ratio, $\delta \sim ab(J_F/K)^{1/2}$, (where J_F is the strength of the exchange interaction, K is the magnetocrystalline anisotropy energy, b is the Fe atomic lattice spacing, and the constant a depends on details of the internal spin structure of the domain wall). From generally accepted values for bulk Fe ($J_F \sim 100$ meV, $K \sim 4$ μeV/atom, $b = 0.287$ nm, $a \sim 10$) one expects that domain walls are a few hundred nm wide. However, SPLEEM images taken after completion of the whole trilayer reveal dramatically different micromagnetic pattern in the thin Fe capping layer (Figs. 10c, 10d) with remarkably thin domain walls.

Interestingly, large regions of the top layer are covered with convoluted magnetic domains separated by 180° domain walls that have complex, meandering structures and uniaxial anisotropy, even though the crystal structure of this system has fourfold symmetry. The capability of SPLEEM to monitor in situ preparation of stacks of magnetic layers without losing the region of interest reveals the origin of this uniaxial anisotropy. Figure 10 shows how the observation that the top Fe layer "chooses" one of the two degenerate easy axes ([010] and [100]) and "ignores" the other one is a consequence of interfacial exchange coupling [127]: the two ferromagnetic layers are magnetically coupled through the NiO spacer (see replication of the large magnetic domains and straight domain walls in the two Fe layers). These results validate the interpretation that, within the NiO grown on top of the Fe substrate film, the antiferromagnetic easy axis latches onto the Fe magnetization direction via antiferromagnetic/ferromagnetic interfacial exchange coupling. When the NiO spacer is covered with the second Fe layer, exchange coupling at this upper interface results in the stabilization of a preferred axis of magnetization that is collinear with the magnetization of the substrate Fe film, although the sign of the magnetization direction is lost. Thus, the antiferromagnetic domains in the NiO spacer scramble the coupling direction with respect to the subsequently deposited Fe layer, but conserve the magnetization axis of the underlying domain in the Fe substrate layer.

Another key observation is the extremely small width of domain walls in the top Fe layer. These domain walls are at least one order of magnitude narrower than the size of 180° walls in the buried Fe layer; their widths are so small that, given the resolution of the SPLEEM images, one can only estimate an upper limit of a few tens of nanometers. In many cases, diameters of the entire domains are even smaller than the widths of domain walls in the bulk-like buried Fe film. Clearly, description of the magnetic pattern in the Fe top layer of these structures is not compatible with conventional models of domain walls [1]. The extremely small width of domain walls in

the top Fe layer can be understood as a consequence of exchange coupling at the ferromagnetic/antiferromagnetic interfaces [127]. Frustrated exchange forces at such interfaces can be far greater than anisotropy forces, and favor the stabilization of domain walls that are narrower than conventional domain walls by a substantial factor. Reference [75] shows how one can estimate the strength of the interfacial exchange coupling, α_u, by measuring the minimum radius $r_{\rm min}$ of magnetic domains in the top Fe layer. The basic idea is to consider a circular, uniformly magnetized domain in the Fe overlayer, fully surrounded by a domain of opposite magnetization. The circular domain wall separating the two magnetic domains is associated with an energetic cost that is proportional to the length of the wall, i.e., it is a function of the domain's radius r. This energy $E_{\rm DW}(r)$ provides a driving force favoring collapse of the domain. A driving force that may prevent collapse and stabilize small domains is exchange coupling at the Fe/NiO interface in the footprint of the domain. The value of this exchange coupling energy $E_{\rm Fe/NiO}$ is a function of the domain size, and it is also a function of the local distribution of interfacial spin structure in the footprint of the domain. When a small domain is stable enough to be observed in the SPLEEM, the exchange coupling energy $E_{\rm Fe/NiO}$ in the footprint of the domain must be sufficiently large to balance the domain wall energy $E_{\rm DW}$. In this picture, it is plausible that a critical radius $r_{\rm min}$ exists, below which any domain would collapse under the pressure of the domain wall energy, even when the local distribution of interfacial spin structure favors the magnetization direction of the domain. According to this argument, for the smallest observed magnetic domains the equality $E_{\rm DW}(r_{\rm min}) = E_{\rm Fe/NiO}(r_{\rm min})$ holds. Invoking a theoretical model [127] describing the strengths of these forces at this type of interface, and solving the equation result in a prediction of how $r_{\rm min}$ depends on the thickness of the top ferromagnetic layer and on the strength of the interfacial exchange coupling α_u [75]. Comparing the predicted dependence with SPLEEM measurements of the critical domain radius $r_{\rm min}$ therefore permits the determination of an experimental estimate of α_u. Variation of minimum domain size with thickness of the Fe capping layer (Figs. 11a, 11b) has been measured using fractal dimension analysis as well as pair correlation analysis of SPLEEM images. A best-fit of the predicted functional dependence with the experimental data, as reproduced in Figure 11c, gives an estimated value of the interfacial exchange coupling $\alpha_u = (1.1 \pm 0.3) \pm 10^{-2}$ [75].

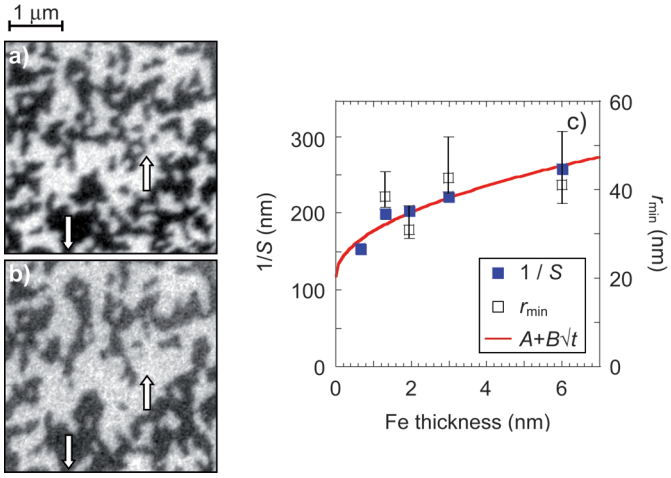

Fig. 11. (Color online) From reference [75] with permission. 4×4 μm SPLEEM images of a Fe(t nm)/NiO(4.5 nm)/Fe(001) trilayer with (a) $t = 1.3$ nm and (b) $t = 6$ nm. These two images show domain coarsening as the thickness of the Fe top layer increases. Local magnetization is given by direction of the white arrows. (c) Inverse of slope S of pair correlation functions and minimum radius $r_{\rm min}$ of stable magnetic domains as a function of thickness t (see text and Ref. [75] for more details). Error bars are indicated for $r_{\rm min}$. Solid line: $r_{\rm min} = A + B\sqrt{t}$ best fit which allows relative adjustment of the two vertical scales and estimation of strength of interfacial exchange coupling.

6 Electron spectroscopy with SPLEEM

In a SPLEEM microscope, the direction of spin polarization and the energy of the incident electron beam can be adjusted. However, the minimum energy these electrons can have in a material is defined by the work function of the surface, 4 to 5 eV is typical for many materials. If the energy of the incident electron beam is smaller than the work function, the beam gets totally reflected (mirror mode) above the sample surface. SPLEEM is thus exclusively sensitive to the electronic structure a few eV above Fermi-level, i.e. SPLEEM only probes unoccupied electronic states. In that sense, it is an interesting complementary tool to photoemission techniques, which address electronic structure below Fermi energy. In this section, we review examples how SPLEEM can be used for spectroscopy purposes, in particular to measure the unoccupied band structure of magnetic or non-magnetic materials, and to probe the electronic properties of buried magnetic interfaces.

When an electron beam hits the surface of a single crystal, part of the beam is reflected while a certain fraction, depending on the electronic band structure in the material (see Sect. 2.2), enters the crystal. If an ultrathin film is epitaxially grown on a single crystal, part of the incident electron beam is also reflected at the interface between the two materials. Depending on the energy ε of the injected electron beam and on the thickness d of the film, beams reflected at the vacuum/film interface and at the film/substrate interface may interfere, giving rise to constructive or destructive interference fringes. This interference effect is analogous to an optical Fabry-Pérot interferometer [77].

This quantum well (QW) effect is illustrated in Figures 12a, 12b where the electron reflectivity of an in situ grown Cu/Co(5 ML)/Cu(001) multilayer is plotted as a function of the incident electron energy and thickness of the Cu top layer [77]. Interference effects are clearly observed after normalizing the measurements by the reflection curve obtained from bulk-like Cu film that does not show quantum well states. In these plots, bright and dark

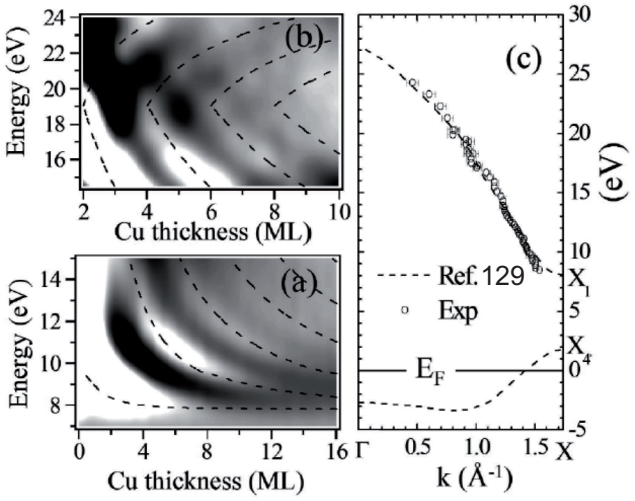

Fig. 12. From reference [77] with permission. (a, b) Electron reflectivity from the Cu surface in a Cu(t ML)/Co(5 ML)/Cu(001) layered structure, with t ranging from 0 to 16 ML and incident energy varying between 7 and 24 eV. Dashed lines in these two plots represent predictions derived from equations (3) and (4). (c) Cu band structure deduced experimentally from (a, b), compared with theoretical calculations of reference [129].

regions correspond to high and low reflectivity, respectively. To model these QW effects, the authors of reference [77] define the complex reflectivities $R_{\rm surf}$ at the surface (Cu/vacuum interface) and $R_{\rm int}$ at the Cu/Co interface: $R_{\rm surf} = r_{\rm surf}\exp(i\Phi_{\rm surf})$ and $R_{\rm int} = r_{\rm int}\exp(i\Phi_{\rm int})$, where r and Φ are the magnitude and phase gain of the electron reflection at the corresponding interfaces. Then the total electron reflectivity can be written:

$$R = \frac{r_{\rm surf}^2 + r_{\rm int}^2 + 2r_{\rm surf}r_{\rm int}\cos(2kd_{\rm Cu} + \Phi_{\rm surf} + \Phi_{\rm int})}{1 + r_{\rm surf}^2 r_{\rm int}^2 + 2r_{\rm surf}r_{\rm int}\cos(2kd_{\rm Cu} + \Phi_{\rm surf} + \Phi_{\rm int})}. \quad (2)$$

In this equation, $d_{\rm Cu}$ is the Cu film thickness and k is the electron momentum vector in the Cu film. The overall reflectivity then oscillates when ε or d is varied, and is maximum when the following quantization condition is fulfilled:

$$2k(\varepsilon)d_{\rm Cu} + \Phi(\varepsilon) = 2\pi n, \quad (3)$$

where n is an integer (number of nodes of the electron wave function) and $\Phi(\varepsilon) = \Phi_{\rm surf} + \Phi_{\rm int}$. If the phase Φ is unknown and energy dependent, it can be eliminated from the quantization condition by choosing an appropriate energy for which this equation is verified for two (d, n) pairs. The quantization equation then becomes $k(\varepsilon) = \pi(n_1 - n_2)/(d_1 - d_2)$. The wave vector k can be measured as a function of ε, i.e. the dispersion relation is obtained.

The electron wave interacts with the QW and with the lattice periodic potential in the Cu film. As a result, Bloch waves that propagate in the film have an envelope function [128]. The quantization equation described above is thus valid for wave vector smaller than half of the Brillouin zone wave vector k_B. For larger k, this equation has to be rewritten:

$$2(k_B - k)d_{\rm Cu} - \Phi(\varepsilon) = 2\pi m, \quad (4)$$

where m is the number of nodes of the envelope function. These two quantization conditions lead an opposite energy vs. thickness dispersion relation, with a crossover for $k = k_B/2$. For Cu, in the (ΓX) direction, theoretical work predicts that the crossover occurs around 19 eV [129]. This crossover is found in the SPLEEM measurements (Fig. 12b). Figure 12c shows the Cu band structure (open circles) derived from the oscillations of the reflectivity with energy and Cu thickness reported in Figures 12a, 12b. For comparison, experimental data are plotted together with band structure calculation of reference [129] (dashed line).

The study of QW resonances can be particularly interesting with spin-polarized electrons. When one looks at a ferromagnetic film, the reflectivity depends on the relative orientation of the incoming spin polarization and local direction of magnetization. In other words, QW resonances are spin-dependent. Using the same procedure as described for the Cu top layer in Cu/Co/Cu(001) samples, the spin-resolved band structure of a ferromagnetic material can be measured. Zdyb and Bauer originally used this procedure to measure the unoccupied band structure of Fe, after growing Fe thin films on W(110) [80]. In particular, the authors have determined the unoccupied, exchange-split band structure of Fe in the (ΓN) direction. These results highlight that, in addition to topography and magnetic images, SPLEEM can also be used to obtain quantitative spectroscopy information.

In the case of Cu/Co(5 ML)/Cu(001) multilayer, the Cu/Co interface separates a noble metal and a ferromagnetic material. Consequently, the reflectivity $R_{\rm int}$ is expected to be spin-dependent, and the Fabry-Pérot interferometer should also be spin-selective. This effect is indeed visible in SPLEEM images (Fig. 13). Comparing reflectivity data of Co(5 ML)/Cu(001) (Fig. 13a) and Cu/Co(5 ML)/Cu(001) (Figs. 13b, 13c) samples, the contributions coming from the ferromagnetic layer alone and from the QW can be distinguished. For the uncapped Co film (Fig. 13a), the magnetic contrast between the two domains varies when increasing the injection energy, but does not change sign. When the same Co film is capped with a 6 ML-thick Cu film (Fig. 13b) the way the magnetic contrast changes as a function of energy is different. In particular, the sign of the spin asymmetry changes with energy, supporting the spin-dependent nature of the Fabry-Pérot interference in the Cu film. This work highlights that, although SPLEEM is a very surface sensitive technique, interfaces buried below several monolayers of material still contribute substantially to the reflected intensity. This shows that SPLEEM can be used to image magnetic microstructure in ferromagnetic films capped with a non-magnetic material or to study electronic properties of buried magnetic interfaces.

This capability can be used to study basic phenomena related to spintronics applications. For example, ultrathin MgO films deposited on a Fe(001) surface have

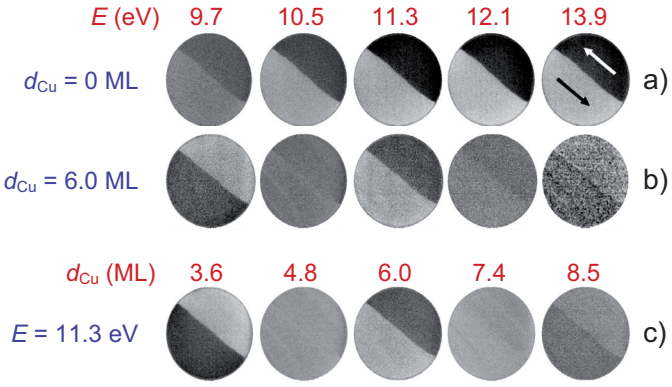

Fig. 13. (Color online) From reference [77] with permission. SPLEEM images illustrating the spin-dependence of Fabry-Pérot interferences in the Cu top layer of Cu/Co(5 ML)/Cu(001) trilayers. (a) Evolution of magnetic contrast in a Co(5 ML)/Cu(001) film for different electron energies. (b) Evolution of magnetic contrast at the same location on the surface after deposition of a 6 ML-thick Cu layer on the Co(5 ML)/Cu(001) film. (c) Evolution of magnetic contrast at the same location on the surface as a function of thickness of the Cu top layer, for a 11.3 eV electron beam. SPLEEM contrast in (b) and (c) shows that both magnitude and sign of the electron reflection asymmetry oscillate with electron energy and Cu film thickness. Arrows in (a) indicate local direction of magnetization in the Co layer. Field of view is 7 μm.

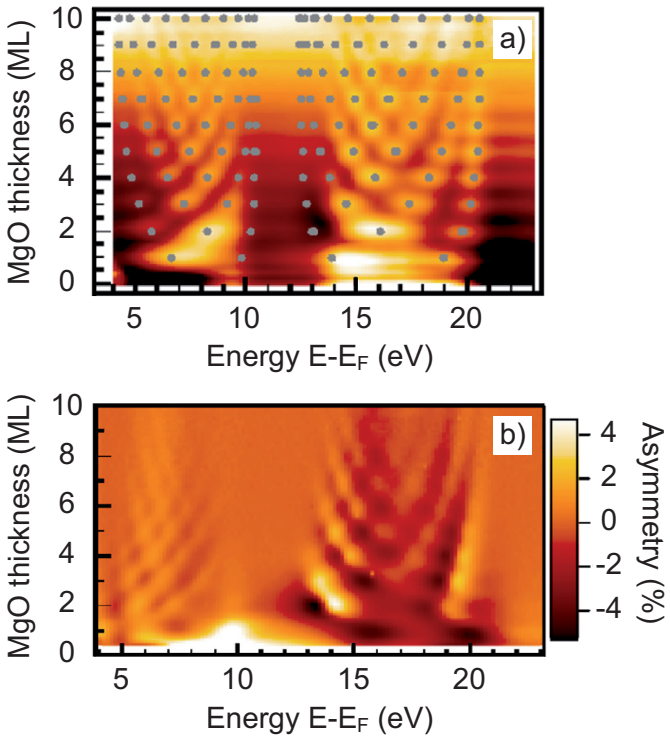

Fig. 14. (Color online) From reference [78] with permission. Quantum well states in MgO thin films grown on Fe(001). (a) Reflectivity and (b) spin asymmetry as a function of MgO thickness and kinetic energy of the incoming electrons. Oscillations of these two quantities are related to the quantum well states in the MgO thin film. Due to the spin-dependence of the reflectivity at the MgO/Fe(001) interface, these quantum well states are spin-polarized.

been shown to be very promising candidates for magnetic tunnel junctions as they exhibit very high tunneling magnetoresistance (TMR). In fact, TMR ratios of ∼200% have been observed at room temperature in Fe/MgO/Fe magnetic tunnel junctions [130,131], and TMR ratios of about 1000% have been predicted theoretically [132,133]. These effects are related to the electronic properties of the MgO barrier, and to support the use of MgO in spintronics applications it is useful to measure its electronic structure experimentally, especially in ultrathin films and structures.

SPLEEM was used to study the MgO/Fe(001) interface during in situ deposition of the MgO layers. SPLEEM images were taken in real time, while scanning the energy of the incident electron beam. As expected, MgO is found to grow pseudomorphically, in a layer by layer manner. Figure 14 shows, for a thin MgO film deposited on a Fe(001) single crystal, the reflectivity (Fig. 14a) and its spin asymmetry (Fig. 14b) as a function of the electron energy and MgO film thickness [78]. Note that spin-dependent QW states are found in the oxide overlayer, although MgO is not magnetic. Similar to the case of a (non-magnetic) Cu layer grown on top of a Co/Cu(001) film, the reflectivity at the buried MgO/Fe interface is spin-dependent. The spin-dependent QW states are still observed up to 10 MgO monolayers, highlighting the capability of SPLEEM to image buried interfaces. Interestingly, the SPLEEM-based band-structure measurements show that even films as thin as 3 ML (not shown here) are electronically very similar to bulk MgO.

7 Summary and outlook

Spin-polarized low-energy electron microscopy is a magnetic imaging method based on the spin-dependence of the elastic backscattering of slow electrons from ferromagnetic surfaces. The possibility to manipulate spin polarization of the electron beam in all spatial directions allows accurate and comprehensive determination of magnetic domain microstructures. As a non-scanning, full-field imaging technique, SPLEEM combines the high performance potential of low-energy electron microscopy with good magnetic sensitivity: spatial resolution, image acquisition rate, energy resolution, the sensitivity to surface composition and structure, and the capability to image samples in real time during in situ processing have made SPLEEM a valuable tool for surface and thin-film magnetism research.

Currently, dramatic advances in electron-optical techniques are becoming available and we can anticipate substantial performance leaps in this type of microscopy. The recent construction of a high-brightness/high-polarization electron source will permit enhanced imaging rates [36, 37]. The possibility to combine improved electron source performance with solid state pixel detectors replacing

multichannelplate image amplifiers with background-free detectors with an unlimited dynamic range [134], promises enhanced capabilities for observation of time-dependent phenomena. Moreover, mirror-based aberration correction techniques are now possible [35,89–91] and it is expected that implementation of these advances will improve spatial resolution by a substantial margin over currently available instruments. Exceeding the limitations of previous imaging optical methods, aberration-corrected SPLEEM may permit 3D vector-magnetometric measurements with 2 nm resolution. Reaching micromagnetic imaging resolution that is of the same length scale as the range of the exchange interaction in many ferromagnetic materials is an exciting prospect for SPLEEM research.

We gratefully acknowledge support by the *Délégation Générale pour l'Armement* under Contract No. 9860830051 (NR) and by the US Department of Energy, Office of Basic Energy Sciences, Division of Materials Sciences and Engineering under Contract No. DEAC02-05CH11231 (AKS).

References

1. A. Hubert, R. Schäfer, *Magnetic Domains: The analysis of magnetic microstructures* (Springer, Berlin, 1998)
2. M.R. Freeman, B.C. Choi, Science **294**, 1484 (2001)
3. E. Betzig, J.K. Trautman, R. Wolfe, E.M. Gyorgy, P.L. Finn, M.H. Kryder, C.-H. Chang, Appl. Phys. Lett. **61**, 142 (1992)
4. B.E. Argyle, J.G. McCord, J. Appl. Phys. **87**, 6487 (2000)
5. M.R. Scheinfein, J. Unguris, M.H. Kelley, D.T. Pierce, R.J. Celotta, Rev. Sci. Instrum. **61**, 2501 (1990)
6. H.P. Oepen, H. Hopster, in *Magnetic Microscopy of Nanostructures*, edited by H. Hopster, H.P. Oepen (Springer, Berlin, 2005), pp. 137–167
7. S. McVitie, J.N. Chapman, L. Zhou, L.J. Heyderman, W.A.P. Nicholson, J. Magn. Magn. Mater. **148**, 232 (1995)
8. A.K. Petford-Long, J.N. Chapman, in *Magnetic Microscopy of Nanostructures*, edited by H. Hopster, H.P. Oepen (Springer, Berlin, 2005), pp. 67–86
9. A. Tonomura, T. Matsuda, H. Tanabe, N. Osakabe, J. Endo, A. Fukuhara, K. Shinagawa, H. Fujiwara, Phys. Rev. B **25**, 6799 (1982)
10. P.A. Midgley, R.E. Dunin-Borkowski, Nat. Mater. **8**, 271 (2009)
11. A. Thiaville, J. Miltat, J.M. García, in *Magnetic Microscopy of Nanostructures*, edited by H. Hopster, H.P. Oepen (Springer, Berlin, 2005), pp. 225–251
12. L. Abelmann, A. van den Bos, C. Lodder, in *Magnetic Microscopy of Nanostructures*, edited by H. Hopster, H.P. Oepen (Springer, Berlin, 2005), pp. 253–283
13. M. Bode, R. Wiesendanger, in *Magnetic Microscopy of Nanostructures*, edited by H. Hopster, H.P. Oepen (Springer, Berlin, 2005), pp. 203–223
14. W.H. Rippard, R.A. Buhrman, Appl. Phys. Lett. **75**, 1001 (1999)
15. W.H. Rippard, R.A. Buhrman, Phys. Rev. Lett. **84**, 971 (2000)
16. P. Fischer, G. Denbeaux, H. Stoll, A. Puzic, J. Raabe, F. Nolting, T. Eimuller, G. Schutz, J. Phys. IV France **104**, 471 (2003)
17. S. Anders, H.A. Padmore, R.M. Duarte et al., Rev. Sci. Instrum. **70**, 3973 (1999)
18. T. Warwick, K. Franck, J.B. Kortright, G. Meigs et al., Rev. Sci. Instrum. **69**, 2964 (1998)
19. J. Raabe, G. Tzvetkov, U. Flechsig, M. Boge et al., Rev. Sci. Instrum. **79**, 113704 (2008)
20. C.F. Hirjibehedin, C.-Y. Lin, A.F. Otte, M. Ternes, C.P. Lutz, B.A. Jones, A.J. Heinrich, Science **317**, 1199 (2007)
21. S. Heinze, M. Bode, A. Kubetzka, O. Pietzsch, X. Nie, S. Blügel, R. Wiesendanger, Science **288**, 1805 (2000)
22. B. Hillebrands, K. Ounadjela (eds.), Spin Dynamics in Confined Magnetic Structures I, in *Topics in Applied Physics*, volume 83 (Springer-Verlag, Berlin, 2002)
23. W. Kuch, J. Vogel, J. Camarero, K. Fukumoto, Y. Pennec, S. Pizzini, M. Bonfim, J. Kirschner, Appl. Phys. Lett. **85**, 440 (2004)
24. J. Vogel, W. Kuch, J. Camarero, K. Fukumoto, Y. Pennec, M. Bonfim, S. Pizzini, F. Petroff, A. Fontaine, J. Kirschner, J. Appl. Phys. **95**, 6533 (2004)
25. A. Vansteenkiste, K.W. Chou, M. Weigand, M. Curcic et al., Nat. Phys. **5**, 332 (2009)
26. F. Cheynis, A. Masseboeuf, O. Fruchart, N. Rougemaille, J.-C. Toussaint, R. Belkhou, P. Bayle-Guillemaud, A. Marty, Phys. Rev. Lett. **102**, 107201 (2009)
27. F. Junginger, M. Kläui, D. Backes, U. Rüdiger, T. Kasama, R.E. Dunin-Borkowski, L.J. Heyderman, Appl. Phys. Lett. **90**, 132506 (2007)
28. P.-O. Jubert, M. Kläui, A. Bischof, J. Appl. Phys. **99**, 08G523 (2006)
29. W. Telieps, E. Bauer, Ultramicroscopy **17**, 57 (1985)
30. W. Telieps, E. Bauer, Surf. Sci. **162**, 163 (1985)
31. M.S. Altman, H. Pinkvos, J. Hurst, H. Poppa, H. Marx, E. Bauer, Mat. Res. Soc. Symp. Proc. **232**, 125 (1991)
32. H. Pinkvos, H. Poppa, E. Bauer, J. Hurst, Ultramicroscopy **47**, 339 (1992)
33. T. Duden, E. Bauer, Rev. Sci. Instrum. **66**, 2861 (1995)
34. K. Grzelakowski, E. Bauer, Rev. Sci. Instrum. **67**, 742 (1996)
35. Elmitec Elektronenmikroskopie GmbH, Germany, `http://www.elmitec-gmbh.com`
36. N. Yamamoto, T. Nakanishi, A. Mano, Y. Nakagawa et al., J. Appl. Phys. **103**, 064905 (2008)
37. M. Suzuki, M. Hashimoto, T. Yasue, T. Koshikawa et al., Appl. Phys. Express **3**, 026601 (2010)
38. E. Bauer, in *Magnetic Microscopy of Nanostructures*, edited by H. Hopster, H.P. Oepen (Springer, Berlin, 2005), pp. 111–136
39. E. Bauer, in *Modern Techniques for Characterizing Magnetic Materials*, edited by Y. Zhu (Kluwer, Boston, 2005), pp. 361–382
40. M.S. Altman, J. Phys.: Condens. Matter **22**, 084017 (2010)
41. T. Scheunemann, R. Feder, J. Henk, E. Bauer, T. Duden, H. Pinkvos, H. Poppa, K. Wurm, Solid State Commun. **104**, 787 (1997)
42. T. Duden, R. Zdyb, M. Altman, E. Bauer, Surf. Sci. **480**, 145 (2001)
43. B. Santos, E. Loginova, A. Mascaraque, A.K. Schmid, K.F. McCarty, J. de la Figuera, J. Phys.: Condens. Matter **21**, 314011 (2009)

44. M.S. Altman, H. Pinkvos, E. Bauer, J. Magn. Soc. Jpn **19**, 129 (1995)
45. E. Bauer, T. Duden, H. Pinkvos, H. Poppa, K. Wurm, J. Magn. Magn. Mater. **156**, 1 (1996)
46. E. Bauer, T. Duden, R. Zdyb, J. Phys. D: Appl. Phys. **35**, 2327 (2002)
47. E. Bauer, R. Belkhou, S. Cherifi, R. Hertel, S. Heun, A. Locatelli, A. Pavlovska, R. Zdyb, N. Agarwal, H. Wang, Surf. Interface Anal. **38**, 1622 (2006)
48. P. Biagioni, A. Brambilla, M. Portalupi, N. Rougemaille, A.K. Schmid, A. Lanzara, P. Vavassori, M. Zani, M. Finazzi, L. Duò, F. Ciccacci, J. Magn. Magn. Mater. **290-291**, 153 (2005)
49. A. Brambilla, P. Biagioni, N. Rougemaille, A.K. Schmid, A. Lanzara, L. Duò, F. Ciccacci, M. Finazzi, Thin Solid Films **515**, 712 (2006)
50. H.F. Ding, A.K. Schmid, Dongqi Li, K.Yu. Guslienko, S.D. Bader, Phys. Rev. Lett. **94**, 157202 (2005)
51. H.F. Ding, A.K. Schmid, D.J. Keavney, Dongqi Li, R. Cheng, J.E. Pearson, F.Y. Fradin, S.D. Bader, Phys. Rev. B **72**, 35413 (2005)
52. J. Choi, J. Wu, F. El Gabaly, A.K. Schmid, C. Hwang, Z.Q. Qiu, New J. Phys. **11**, 043016 (2009)
53. T. Duden, E. Bauer, Phys. Rev. Lett. **77**, 2308 (1996)
54. T. Duden, E. Bauer, MRS Symp. Proc. **475**, 283 (1997)
55. T. Duden, E. Bauer, J. Electron Microsc. **47**, 379 (1998)
56. T. Duden, E. Bauer, Surf. Rev. Lett. **5**, 1213 (1998)
57. T. Duden, E. Bauer, J. Magn. Magn. Mater. **191**, 301 (1999)
58. T. Duden, E. Bauer, Phys. Rev. B **59**, 474 (1999)
59. T. Duden, E. Bauer, Phys. Rev. B **59**, 468 (1999)
60. M. Finazzi, A. Brambilla, P. Biagioni, J. Graf, G.H. Gweon, A. Scholl, A. Lanzara, L. Duò, Phys. Rev. Lett. **97**, 097202 (2006)
61. F. El Gabaly, S. Gallego, C. Munoz, L. Szunyogh, P. Weinberger, C. Klein, A.K. Schmid, K.F. McCarty, J. de la Figuera, Phys. Rev. Lett. **96**, 147202 (2006)
62. F. El Gabaly, K. McCarty, A.K. Schmid, J. de la Figuera, M.C. Munoz, L. Szunyogh, P. Weinberger, S. Gallego, New J. Phys. **10**, 073024 (2008)
63. J. Graf, C. Jozwiak, A.K. Schmid, Z. Hussain, A. Lanzara, Phys. Rev. B **71**, 144429 (2005)
64. K. Grzelakowski, T. Duden, E. Bauer, H. Poppa, Chiang, IEEE Trans. Magn. **30**, 4500 (1994)
65. C. Klein, R. Ramchal, M. Farle, A.K. Schmid, Surf. Interface Anal. **38**, 1550 (2006)
66. C. Klein, R. Ramchal, A.K. Schmid, M. Farle, Phys. Rev. B **75**, 193405 (2007)
67. K.L. Man, M.S. Altman, H. Poppa, Surf. Sci. **480**, 163 (2001)
68. K.L. Man, R. Zdyb, S.F. Huang, T.C. Leung, C.T. Chan, E. Bauer, M.S. Altman, Phys. Rev. B **67**, 184402 (2003)
69. R.J. Phaneuf, A.K. Schmid, Phys. Today **56**, 50 (2003)
70. H. Pinkvos, H. Poppa, E. Bauer, G.-M. Kim, in *Magnetism and Structure in Systems of Reduced Dimension*, edited by R.F.C. Farrow, B. Dieny, M. Donath, A. Fert, B.D. Hermsmeier (Plenum Press, New York, 1993), p. 25
71. H. Poppa, E.D. Tober, A.K. Schmid, J. Appl. Phys. **91**, 6932 (2002)
72. R. Ramchal, A.K. Schmid, M. Farle, H. Poppa, Phys. Rev. B **68**, 054418 (2003)
73. R. Ramchal, A.K. Schmid, M. Farle, H. Poppa, Phys. Rev. B **69**, 214401 (2004)
74. N. Rougemaille, A.K. Schmid, J. Appl. Phys. **99**, 08S502 (2006)
75. N. Rougemaille, M. Portalupi, A. Brambilla, P. Biagioni, A. Lanzara, M. Finazzi, A.K. Schmid, L. Duò, Phys. Rev. B **76**, 214425 (2007)
76. E.D. Tober, G. Witte, H. Poppa, J. Vac. Sci. Technol. A **18**, 1845 (2000)
77. Y.Z. Wu, A.K. Schmid, M.S. Altman, X.F. Jin, Z.Q. Qiu, Phys. Rev. Lett. **94**, 027201 (2005)
78. Y.Z. Wu, A.K. Schmid, Z.Q. Qiu, Phys. Rev. Lett. **97**, 217205 (2006)
79. Y.Z. Wu, Z.Q. Qiu, A.K. Schmid, J. Magn. Magn. Mater. **310**, 1629 (2007)
80. R. Zdyb, E. Bauer, Phys. Rev. Lett. **88**, 166403 (2002)
81. R. Zdyb, E. Bauer, Surf. Rev. Lett. **9**, 1485 (2002)
82. R. Zdyb, E. Bauer, Phys. Rev. B **67**, 134420 (2003)
83. R. Zdyb, A. Locatelli, S. Heun, S. Cherifi, R. Belkhou, E. Bauer, Surf. Interface Anal. **37**, 239 (2005)
84. R. Zdyb, A. Pavlovska, M. Jałochowski, E. Bauer, Surf. Sci. **600**, 1586 (2006)
85. R. Zdyb, E. Bauer, Phys. Rev. Lett. **100**, 155704 (2008)
86. R. Zdyb, A. Pavlovska, A. Locatelli, S. Heun, S. Cherifi, R. Belkhou, E. Bauer, Appl. Surf. Sci. **249**, 38 (2005)
87. R. Zdyb, T.O. Mentes, A. Locatelli, M.A. Nino, E. Bauer, Phys. Rev. B **80**, 184425 (2009)
88. R. Zdyb, A. Pavlovska, E. Bauer, J. Phys.: Condens. Matter **21**, 314012 (2009)
89. Th. Schmidt, U. Groh, R. Fink, E. Umbach et al., Surf. Rev. Lett. **9**, 223 (2002)
90. W. Wan, J. Feng, H.A. Padmore, D.S. Robin, Nucl. Instrum. Meth. Phys. Res. A **519**, 222 (2004)
91. Specs GmbH, Germany, `http://www.specs.de/cms/front_content.php?idart=499`
92. E. Bauer, Rep. Prog. Phys. **57**, 895 (1994)
93. E. Bauer, J. Phys.: Condens. Matter **21**, 314001 (2009)
94. F. Meier, B.P. Zakharchenya, *Optical Orientation, Modern problems in Condensed Matter Sciences*, edited by V.M. Agranovich, A.A. Maradudin (North-Holland, Amsterdam, 1984), Vol. 8
95. C. Hermann, G. Lampel, Ann. Phys. (Paris) **10**, 1117 (1985)
96. D.T. Pierce, F. Meier, P. Zürcher, Appl. Phys. Lett. **26**, 670 (1975)
97. Yu. Mamaev, H.-J. Drouhin, G. Lampel, A. Subashiev, Yu. Yashin, A. Rochansky, J. Appl. Phys. **93**, 9620 (2003)
98. M.P. Seah, W.A. Dench, Ann. Phys. **1**, 2 (1979)
99. S. Tanuma, C.J. Powell, D.R. Penn, J. Vac. Sci. Technol. A **8**, 2213 (1990)
100. D.P. Pappas, K.-P. Kämper, B.P. Miller, H. Hopster, D.E. Fowler, C.R. Brundle, A.C. Luntz, Z.-X. Shen, Phys. Rev. Lett. **66**, 504 (1991)
101. M. Getzlaff, J. Bansmann, G. Schönhense, Solid State Commun. **87**, 467 (1993)
102. G. Schönhense, H.C. Siegmann, Ann. Phys. (Leipzig) **2**, 465 (1993)
103. R. Allenspach, M. Stampanoni, A. Bischof, Phys. Rev. Lett. **65**, 3344 (1990)
104. M. Speckmann, H.P. Oepen, H. Ibach, Phys. Rev. Lett. **75**, 2035 (1995)
105. S. Müller, B. Schulz, G. Kostka, M. Farle, K. Heinz, K. Baberschke, Surf. Sci. **364**, 235 (1996)

106. M. Farle, Rep. Prog. Phys. **61**, 755 (1998)
107. W.L. O'Brien, B.P. Tonner, Phys. Rev. B **49**, 15370 (1994)
108. M. Farle, B. Mirwald-Schulz, A.N. Anisimov, W. Platow, K. Baberschke, Phys. Rev. B **55**, 3708 (1997)
109. M. Farle, W. Platow, A.N. Anisimov, P. Poulopoulos, K. Baberschke, Phys. Rev. B **56**, 5100 (1997)
110. V. Jähnke, J. Güdde, E. Matthias, J. Magn. Magn. Mater. **237**, 69 (2001)
111. Each anisotropy coefficient is the sum of a volume contribution and a thickness-dependent surface contribution
112. B. Heinrich, T. Monchesky, R. Urban, J. Magn. Magn. Mater. **236**, 339 (2001)
113. K. Wagner, N. Weber, H.J. Elmers, U. Gradmann, J. Magn. Magn. Mater. **167**, 21 (1997)
114. U. Gradmann, J. Korecki, G. Waller, Appl. Phys. A **39**, 101 (1986)
115. D. Sander, R. Skomski, A. Enders, C. Schmidthals, D. Reuter, J. Kirschner, J. Phys. D **31**, 663 (1998)
116. L. Lu, J. Bansmann, K.H. Meiwes-Broer, J. Phys.: Condens. Matter **10**, 2873 (1998)
117. K.F. McCarty, J.C. Hamilton, Y. Sato et al., New J. Phys. **11**, 043001 (2009)
118. U. Gradmann, G. Waller, Surf. Sci. **116**, 539 (1982)
119. O. Fruchart, P.-O. Jubert, M. Eleoui, F. Cheynis, B. Borca, P. David, V. Santonacci, A. Lienard, M. Hasegawa, C. Meyer, J. Phys.: Condens. Matter **19**, 053001 (2007)
120. O. Fruchart, M. Eleoui, J. Vogel, P.-O. Jubert, A. Locatelli, A. Ballestrazzi, Appl. Phys. Lett. **84**, 1335 (2004)
121. H.F. Ding, A.K. Schmid, K.Yu. Gueslyenko, Dongqi Li, S.D. Bader (to be published)
122. M.J. Donahue, D.G. Porter, OOMMF User's Guide Version 1.0 (National Institute of Standards and Technology, Gaithersburg, MD, 1999)
123. I. Žutić, J. Fabian, S. Das Sarma, Rev. Mod. Phys. **76**, 323 (2004)
124. J. Vogel, W. Kuch, R. Hertel, J. Camarero et al., Phys. Rev. B **72**, 220402(R) (2005)
125. M. Hehn, D. Lacour, F. Montaigne, J. Briones, R. Belkhou, S. El Moussaoui, F. Maccherozzi, N. Rougemaille, Appl. Phys. Lett. **92**, 072501 (2008)
126. L. Duò, M. Portalupi, M. Marcon, R. Bertacco, F. Ciccacci, Surf. Sci. **518**, 234 (2002)
127. A.I. Morosov, A.S. Sigov, Phys. Solid State **46**, 395 (2004)
128. Z.Q. Qiu, N.V. Smith, J. Phys.: Condens. Matter **14**, R169 (2002)
129. R. Lässer, N.V. Smith, R.L. Benbow, Phys. Rev. B **24**, 1895 (1981)
130. S. Yuasa, T. Nagahama, A. Fukushima, Y. Suzuki, K. Ando, Nat. Mater. **3**, 868 (2004)
131. S.S.P. Parkin, C. Kaiser, A. Panchula, P.M. Rice, B. Hughes, M. Samant, S.H. Yang, Nat. Mater. **3**, 862 (2004)
132. W.H. Butler, X.-G. Zhang, T.C. Schulthess, J.M. MacLaren, Phys. Rev. B **63**, 054416 (2001)
133. J. Mathon, A. Umerski, Phys. Rev. B **63**, 220403 (2001)
134. R. van Gastel, I. Sikharulidze, S. Schramm, J.P. Abrahams, B. Poelsema, R.M. Tromp, S.J. van der Molen, Ultramicroscopy **110**, 33 (2009)